Gravity Optimised Particle Filter for Hand Tracking

Malik Morshidi, Tardi Tjahjadi

School of Engineering, University of Warwick Gibbet Hill Road, Coventry, CV4 7AL, United Kingdom.

Abstract

This paper presents a gravity optimised particle filter (GOPF) where the magnitude of the gravitational force for every particle is proportional to its weight. GOPF attracts nearby particles and replicates new particles as if moving the particles towards the peak of the likelihood distribution, improving the sampling efficiency. GOPF is incorporated into a technique for hand features tracking. A fast approach to hand features detection and labelling using convexity defects is also presented. Experimental results show GOPF outperforms the standard particle filter and its variants, as well as state-of-the-art Camshift guided particle filter using a significantly reduced number of particles.

*Keywords:*Particle filter, articulated hand tracking, finger movement, gravity, convexity defects, Camshift.

1. Introduction

Among human body parts, the hand is the most effective means of non-verbal communication and plays an effective role in human computer interaction such as gesture recognition [1, 2], virtual reality [3], and computer games [4, 5]. Hand gesture recognition involves hand tracking and the difficulties in developing a hand tracking system include: high dimensionality of the tracking; finger self-occlusion; high processing speed; and rapid hand motion [6]. Hitherto, an accurate and real-time hand tracking system is still far from realised. In this paper we propose an approach which balances the need for real-time requirement and acceptable accuracy. The approach incorporates an improved particle filter for hand tracking and detects hand features by computing the convexity defects of the hand silhouette contour.

The standard particle filter (PF) also known as conditional density propagation (i.e., condensation) algorithm (e.g., [7]) incorporates the use of complex motion models and is highly robust to clutter. However, it lacks the ability to run in real-time since the number of samples (or particles) is large in order to account for sudden movements of the object being tracked. A large number is also needed to overcome the samples impoverishment problem by populating some areas of the state-space that may be left empty due to prediction of the motion model that tends to cluster the samples in some area due to the predicted motion.

The ICondensation algorithm [8], an extension of PF, permits the combination of the original random sampling filter representation with the information available from alternative sensors in the form of an importance function. The importance function aids the sampling from prior method by generating and concentrating samples in areas of the state-space that contain most information about the posterior. This

helps alleviate the samples degeneracy problem by avoiding to generate samples which have low weights to represent the posterior. Samples drawn from the importance function are systematically formulated in such a way that they do not change the probabilistic model of the tracker.

In [9] a local optimiser based on the stochastic meta-descent tracker is integrated after the standard particle propagation step. The new particles generated by the optimiser are combined with the original particles distribution which results in a smart particle filter that can track high-dimensional articulated structure with far fewer particles. In [10], after particles propagation the mean shift embedded particle filter (MSEPF) is applied to move the particles to the nearby local modes with high likelihood resulting in better posterior estimation. Using significantly fewer particles, MSEPF operates robustly and with lesser computational burden. In [11] CamShift Guided Particle Filter (CAMSGPF) employs a simplified version of CamShift which iterates at a smaller and fixed interval to reduce the computational burden. This is unlike CamShift that will iterate until convergence. The optimisation procedure in CAMSGPF takes into account the current observation which results in new proposal density of the current samples for which new samples are drawn.

Since the introduction of PF for object tracking, most of the works derived thereafter evolve around the use of weighted particles to represent the posterior density. In this paper we propose the gravity optimised particle filter (GOPF) that generates a new set of particles based on current observation and allows each weighted particle to have its own gravitational force (from an analogy with Newton's law of universal gravitation) that will attract nearby particles towards the peak of the particles distribution. The newly generated particles is combined with the particles generated in the same way as with a PF. The weights for the new particles depend on their position relative to the current observation to enable the combined particles to maintain the multiple hypotheses nature of the tracker.

There are generally two approaches to hand tracking: model-based and appearance-based. The model-based approach [12, 13] is based on parametric models of the shape and kinematic structure of the 3-dimensional (3D) hand. Using the motion history and dynamics of the hand, this approach predicts the model hypotheses when a new observation is made by measuring the dissimilarity between the expected model hypotheses with the actual observation. However, seeking the optimised solution in a multidimensional model parameters space especially with the complexity of hand motion and self occlusion makes this approach unreliable for long video sequences. Furthermore, the computational requirements is high. Recent work in [12] addresses this poblem using GPU-based software implementation and off-the-shelf Kinect sensor which demonstrates robust 3D articulated hand tracking in near real-time (15Hz) over a long sequence.

The appearance-based approach [14, 15] is based on appearance-specific 2D image mapping from a set of image features to a limited set of predefined poses. The approach is goal-oriented, where a small set of predefined poses needs to be recognised, making it impossible to estimate other poses. Variable length Markov model is combined with annealed PF in [16] to account for discontinuous changes during the

observations. The framework operates by automatic switching between first-order Markov model and PF. The former is used for the case of previously observed events, whereas the later operates for the case of unseen events. In [13], appearance-guided PF is used for high degree-of-freedom (DOF) tracking in image sequences. PF is extended by using state space vectors that act as attractors, and a probability propagation framework is derived to find the approximation for the maximum a posteriori solution. This solution avoids the drifting effect of PF.

In this paper we present a model-based framework for tracking hand features. The framework incorporates GOPF and a fast method for detecting hand features using convexity defects. The main advantage using the proposed hand features detection is due to its reasonable accuracy and fast processing. It also does not depend on offline learning from database of hand features or postures.

This paper is organised as follows: Section 2 provides an overview of the proposed hand tracking framework. Section 3 presents the details of GOPF. Section 4 provides detailed explanation of the measurement model. Finally, Section 6 and Section 7 respectively present the experimental results and conclusions.

2. Overview of the Proposed Hand Tracking Framework

In addition to the weighted particles generated in the same way as with a PF, the proposed hand tracking framework uses GOPF which utilises the gravitational concept to attract nearby particles towards the virtual likelihood particle, i.e., the current observation. The framework involves the combination of the standard PF and GOPF. At every time step, N particles of the $2N$ particles from the previous time step are resampled and propagated based on the PF framework. Using the locations of the N propagated particles as reference, a new set of m particles (where $m < N$) are replicated at where some of the N particles close to the current observation should move due to the attraction effect (referred to as Algorithm 1). Another set of new n particles (where $m + n = N$) are randomly propagated within the expected direction of the next observation (referred to as Algorithm 2). The N, m, and n particles are combined to give the new total of $2N$ particles. This enhances the proposal density of the likelihood distribution while maintaining the original Bayesian distribution of the weighted particles. As the proposal density improves, the need for large number of particles reduces significantly. The framework also incorporates a model for hand features extraction with slight modification on the localisation and labelling of fingers as in [17]. Unlike in [17] where the dominant features are extracted using a k-cosine curvature, we use a faster approach using convexity defect [18]. Tracking the fingertips throughout an image sequence using only the hand features extraction algorithm might not work adequately, especially when the hand encounters partial or complete occlusion. Therefore, GOPF (referred to as Algorithm 3) is incorporated in the framework to boost the stability of the hand tracking when encountering noisy measurements and occlusions.

3. Gravity Optimised Particle Filter (GOPF)

The ability of PF to handle multiple hyphotheses with non-linear motion and non-linear observations has made it the most widely used tracking technique [19, 10, 11, 20]. Object tracking in the PF framework [21, 7] is the process of sequentially estimating the state parameters x_t at time t. Given the set of observations history $Z_t = \{z_1, ..., z_t\}$, the Bayesian formulation of PF is expressed as the computation of posterior probability, i.e.,

$$p(x_t|Z_t) = \eta p(z_t|x_t) \int p(x_t|x_{t-1}) p(x_{t-1}|Z_{t-1}) dx_{t-1}, \tag{1}$$

where η is the normalisation constant, $p(z_t|x_t)$ is the likelihood model, $p(x_t|x_{t-1})$ is the motion model and $p(x_{t-1}|Z_{t-1})$ is the temporal prior. At each time-step t of the PF iteration, the posterior probability is estimated by assigning each particle $s_t^{(n)}$ with a weight $\pi_t^{(n)}$. The weighted particle set $\{(s_t^{(n)}, \pi_t^{(n)}), n = 1, ..., N\}$ represents the hypothetical states of the conditional state-density $p(x_t|Z_t)$ (i.e., the posterior probability) of the object at time t. The best approximation of the state is determined by either the highest weighted particle, or the average of particles' weights. The particles set at the next time-step is resampled and propagated according to the motion model. Computing the posterior probability with an integral over all possible state values [21, 7] in each iteration is computationally infeasible. To alleviate this problem, importance sampling or resampling is used to combine the prior knowledge of the object position and motion with any additional knowledge extracted from auxiliary sensors [8]. Since the dynamics of hand motion is non-linear, we adopt a general motion model of the Gaussian random walk [22]. The measurement in the current image is used to hypothesize the likelihood regions of the state space.

3.1. Theoretical basis of GOPF

Particles in a PF framework can be thought of as point masses of physical bodies in the theory of gravity. Each weighted particle is considered to have an additional property of gravity with a gravitational force proportional to its mass. Newton's law of universal gravitation [23] states that any point mass m_1 attracts every other single point mass m_2 by a force. The two point masses that are attracted towards each other can be viewed as time dependent in which the magnitude of the force at time t, i.e., F_t, becomes greater. This in turn affects the acceleration of a point mass at time t, i.e., a_t, a time dependent acceleration of motion. The computation of the positions of two attracting point masses at time t which considers time dependent acceleration is a time consuming iterative process, where the position of a point mass at time t is

$$l_t = l_0 + u_0 t + \frac{1}{2} a_t t^2, \tag{2}$$

where $a_t = \frac{F_t}{m}$, $F_t = G\frac{m_1 m_2}{r^2}$, G is a gravitational constant and r is the distance between two point masses. For simplicity we assume a_t is a constant acceleration and that every point mass starts at position $l_0 = 0$

with initial velocity $u_0 = 0$, thus the displacement of that point is

$$\Delta l = \frac{1}{2} a_t t^2. \tag{3}$$

3.2. The Implementation of GOPF

GOPF using Algorithm 1 uses the gravitational basis in Section 3.1. After the propagation of the previous time step a new set of particles $\{(g_t^{(c)}, \omega_t^{(c)}), c = 1, ..., C\}$ is generated in accordance with the current observation. Each weighted particle, generated in the same way as with a PF, has its own gravitational force whose magnitude is proportional to its weight. The PF integrated in our work is the condensation algorithm [7] implemented in OpenCV 2.1. We introduce a virtual particle $\bar{s}_T$ for which its state vector is the same as the current observation z_t. The mass of the virtual particle m_T is equal to 1 and is multiplied by a *scale*. Since two small particles would not have significant gravitational effect, the *scale* is set experimentally (normally set to 1000) to increase the effect of the gravitational force. The gravitional effect of every particle $\bar{s}_P^i = s_t^{(n)}$ in $\{(s_t^{(n)}, \pi_t^{(n)}), n = 1, ..., N\}$ is evaluated against the virtual particle $\bar{s}_T$, where N is the number of particles. The weight $\pi_t^{(n)}$ of $s_t^{(n)}$ is first updated based on $p(z_t|x_t = s_t^{(n)})$, and the likelihood function (i.e., weight) is defined as

$$\pi_t^{(n)} = \exp(-0.05 \times r), \tag{4}$$

where r is the distance between the particles $\bar{s}_P^i$ and $\bar{s}_T$, i.e.,

$$r = \left[\sum_{i=1}^{n} (\bar{s}_P^i - \bar{s}_T)^2 \right]^{\frac{1}{2}}. \tag{5}$$

The weight $\pi_t^{(n)}$ is used to set the mass m_P of $\bar{s}_P^i$, which is mutiplied by a factor *scale*.

For every evaluation of the gravitational effect between $\bar{s}_P^i$ and $\bar{s}_T$, two new particles $\bar{g}_P$ and $\bar{g}_T$ are generated if the weight $\pi_t^{(n)}$ is greater than or equal to a certain threshold τ. This is done by replicating where $\bar{s}_P^i$ and $\bar{s}_T$ should move to using $\bar{g}_P$ and $\bar{g}_T$, respectively. The replication process starts by calculating the force F_t and acceleration a_P and a_T (step 8 of Algorithm (1)). If particle $\bar{s}_P^i$ is about to be moved, the acceleration a_P and a_T of $\bar{s}_P^i$ and $\bar{s}_T$, respectively, as well as the force F_t are computed. Assuming a constant acceleration, the positions of $\bar{g}_P$ and $\bar{g}_T$ at any time *tStep* are calculated in advance using (3).

The new particles $\bar{g}_P$ and $\bar{g}_T$ are replicated when the ratio of the total displacement between displacements (i.e., Δl_P of $\bar{s}_P^i$ and Δl_T of $\bar{s}_T$) and distance r are between 70% and 90%. Replicating new particles below than 70% ratio might create sample degeneracy problem, whilst replication at greater than 90% ratio might suffer from sample impoverishment. The cut off ratio, 80%, is selected to avoid sample degeneracy and impoversihment. One way to achieve this is by starting the computation at time *tStep*=0 and gradually increasing the *tStep* by 0.1 as illustrated in the top plot of Fig. 1. The iteration is stopped when the total displacement is greater than 80%. The last *tStep* is used to replicate the new particles. However this process

Algorithm 1 Replicate by gravity.

Generate new set of particles $\{(g_t^{(c)}, \omega_t^{(c)}), c = 1, ..., C\}$ where $C = N$

$\bar{s}_T = z_t$
likelihood mass $m_T = 1 * scale$
for each particle in $\{(s_t^{(n)}, \pi_t^{(n)}), n = 1, ..., N\}$ **do**
  $\bar{s}_P^i = s_t^{(n)}$
  update weight $\pi_t^{(n)} = p(z_t | x_t = s_t^{(n)})$
  particle mass $m_P = \pi_t^{(n)} * scale$
  if $\pi_t^{(n)} \geq$ threshold τ AND $c < C$ **then**
    calculate F_t, a_P, and a_T (Section (3.1))
    $isShifted = 0$
    $tStep = k$
    while NOT $isShifted$ AND $tStep > 0$ **do**
      calculate Δl_P and Δl_T using (3)
      if $(\frac{\Delta l_P + \Delta l_T}{r}) < 0.8$ **then**
        $isShifted =$ TRUE
        $\bar{g}_P = (\bar{s}_T - \bar{s}_P^i) \times (\frac{\Delta l_P}{r}) + \bar{s}_P^i$
        $\bar{\omega}_P$ using (6)
        $\bar{g}_T = (\bar{s}_P^i - \bar{s}_T) \times (\frac{\Delta l_T}{r}) + \bar{s}_T$
        $\bar{\omega}_T$ using (7)
      end if
      $tStep = tStep - 0.1$
    end while
    assign $g_t^{(c)}$, $\omega_t^{(c)}$, $g_t^{(c+1)}$ and $\omega_t^{(c+1)}$, with $\bar{g}_P$, $\bar{\omega}_P$, $\bar{g}_T$ and $\bar{\omega}_T$, respectively
    $c = c + 2$
  else
    Use Algorithm 2
  end if
end for

is time consuming and requires 39 iterations to move two particles with weigths 0.4 and 1 placed at positions x=20 and x=180, respectively to reach a total displacement of greater than 80% with the final $tStep$=3.8. A better way to achieve this is to start the computation at time $tStep$=k, and gradually decreasing $tStep$ by 0.1 until the total displacement is less than 80% as illustrated in the bottom plot of Fig. 1. This time decreasing iteration requires only 1 iteration with $tStep$ starting at 3.0 and is thus preferred. Note that the final locations of the new particles are not the same for both ways. This sub-optimised solution is similar to the work in [10, 11] where the new particles are generated closer but not too close to the local mode. This maintains and improves the original Bayesian distribution of the weighted particles. The new weight $\bar{\omega}_P$ for $\bar{g}_P$ is

$$\omega_t^{(c)} = \pi_t^{(n)} + (\frac{\Delta l_P}{r} \times (1 - \pi_t^{(n)})), \tag{6}$$

whereas the new weight $\bar{\omega}_T$ for $\bar{g}_T$ is

$$\omega_t^{(c)} = 1 - (\frac{\Delta l_T}{r} \times (1 - \pi_t^{(n)})), \tag{7}$$

where Δl_P and Δl_T are calculated using (3).

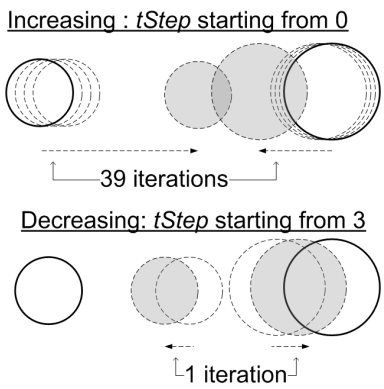

Figure 1: Two modes of attracting particles (denoted by bold circles): (top) time increasing iteration; and (bottom) time decreasing iteration. Shaded circles are the final locations of the replicated particles.

Fig. 2(a) is an example of PF propagation using 10 particles. The particles that fall within the threshold τ from the current observation z_t are evaluated using Algorithm 1. The rest of the particles are evaluated using Algorithm 2. We present a quantitative experiment in Section 6.1 to show what threshold value τ gives GOPF its best performance. Fig. 2(b) is the optimised particles distribution using Algorithm 1 of GOPF. The four borderless grey circles are the new particles replicated based on where the four particles (black circles) should move. The four bordered grey circles near the current observation z_t are other new particles replicated based on where the virtual particle (at z_t) should move. The white bordered circles are the particles propagated by Algorithm 2. Algorithm 1 only replicates the nearby particles. The remaining particles are propagated based on the previous drift (PD) of the object being tracked.

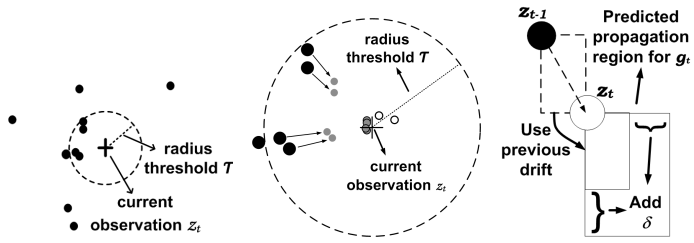

(a) (b) (c)

Figure 2: (a) Selecting particles to be replicated; (b) The optimised particles distribution using Algorithm 1 of GOPF; and (c) Predicted propagation region based on drift (Algorithm 2 of GOPF).

Algorithm 2 Propagate within predicted drift region.

1: **if** $(\Delta\dot{D} = z_t - z_{t-1}) < 0$ **then**
2: $\quad \hat{L} = \Delta\dot{D} - \delta$
3: $\quad \hat{U} = 0$
4: **else**
5: $\quad \hat{L} = 0$
6: $\quad \hat{U} = \Delta\dot{D} + \delta$
7: **end if**
8: **for** $i = c$ to C **do**
9: $\quad g_t^{(i)} = z_t + \tilde{r} \mod (\hat{U} - \hat{L} + 1) + \hat{L}$
10: $\quad$ update weight $\omega_t^{(i)} = p(z_t | x_t = g_t^{(i)})$
11: **end for**

Algorithm 2 summarises the propagation procedure based on the PD region. Fig. 2(c) illustrates the region of possible propagation based on current observation and the PD (indicated by dashed line rectangle), where z_{t-1} and z_t are respectively the locations of the previous and current observations. The PD region is determined by taking the difference $\Delta\dot{D} = \{\Delta\dot{d}_x, \Delta\dot{d}_y\}$ between z_t and z_{t-1} in both horizontal x and vertical y directions. The upper and lower values in both directions, denoted as $\hat{U} = \{\hat{u}_x, \hat{u}_y\}$ and $\hat{L} = \{\hat{l}_x, \hat{l}_y\}$, respectively, are set accordingly. Depending on $\Delta\dot{D}$ direction, $\hat{U}$ or $\hat{L}$ is added (minus for negative direction) with a threshold δ which are then used as an upper and lower bound when propagating $g_t^{(i)}$ with random value $\tilde{r}$ (line 9 of Algorithm 2). The initial value c used in the for loop is the last updated index in Algorithm 1, where $C = N$, is the total number of newly generated particles based on GOPF. The weight for $g_t^{(i)}$ (at line 10 of Algorithm 2) is updated based on the likelihood function defined in (4). GOPF is summarised in Algorithm 3 where at any time step, the first half consisting N particles are resampled and propagated based on the PF framework. During the update stage, new set of particles consisting another N particles are generated either using Algorithm 1 or Algorithm 2. They are then combined producing a total of $2N$

particles, and are used to estimate the next state.

Algorithm 3 The GOPF.

1: Resample $\{s_{t-1}^{'(m)}\}_{m=1}^{N}$ from $\{(s_{t-1}^{(n)}, \pi_{t-1}^{(n)})\}_{n=1}^{2N}$
2: Propagate $s_t^{''(n)} \backsim p(x_t|x_{t-1} = s_{t-1}^{'(m)})$ to give $\{s_t^{''(n)}\}_{n=1}^{N}$
3: Update using Algorithm 1 or Algorithm 2 to give $\{(g_t^{(c)}, \omega_t^{(c)})\}_{c=1}^{N}$ and $\{(s_t^{''(n)}, \pi_t^{(n)})\}_{n=1}^{N}$
4: Combine $\{(g_t^{(c)}, \omega_t^{(c)})\}_{c=1}^{N}$ and $\{(s_t^{''(n)}, \pi_t^{(n)})\}_{n=1}^{N}$ to give $\{(s_t^{(m)}, \pi_t^{(m)})\}_{m=1}^{2N}$
5: Estimate $\hat{s}_t = \sum_{m=1}^{2N} \pi_t^{(m)} s_t^{(m)}$

4. Hand Features Extraction

The approach taken for hand features extraction in this paper is appropriate for a hand interacting with an object while facing the camera and with finger bending one at a time. The frontal hand movement is limited to palm bending within 45° in X, Y and Z axes.

One of the distinctive features of a hand is its skin colour. We adapt the implementation of the skin segmentation for face tracking in [24] for our GOPF based hand tracking framework. With some user interaction in the first video image frame, the skin colour is extracted. As an analysis of skin colour is not in within the scope of our current research, a fully automatic initialisation would be considered as a future work. The input RGB image to the segmentation algorithm is converted into the HSV colour space, and the hue channel I_h is used to represent the image. Skin segmentation is achieved by matching I_h with a normalised skin colour histogram distribution H_{skin} via back projection. The resulting image I_{bp} is a single channel image where each pixel in I_{bp} is a probability value of that characterized by H_{skin}, i.e.,

$$I_{bp} = p(I_h|H_{skin}) = \frac{p(I_h)}{p(H_{skin})} p(H_{skin}|I_h). \tag{8}$$

The largest skin coloured blob is considered to be the hand [12]. A contour is traced on I_{bp} and Douglas-Peucker polygon approximation method [25, 24] is used to reduce the number of redundant contour points cp.

4.1. Locating Potential Finger Valleys

A convex hull based on Sklansky method [26, 24] is implemented for detecting hand contour, and followed by extracting its convexity defects based on Homma's method in [18, 24]. Each convexity defect structure comprises valley/depth point $dp(x, y)$, start point $sp(x, y)$, end point $ep(x, y)$ and depth ld as shown in Fig. 3(a). There are four significant finger valleys denoted by $V = \{v_0, v_1, v_2, v_3\}$ as shown in Fig. 3(b). To detect finger valleys of any hand, the four convexity defect structures with the deepest/longest ld are first selected as temporary finger valleys denoted $\bar{V} = \{\bar{v}_0, \bar{v}_1, \bar{v}_2, \bar{v}_3\}$. Note that the elements of $\bar{V}$ are in

sequential order in anticlockwise direction. The convexity defects 1, 3, 4 and 5 in Fig. 3(a) are selected to be the four convexity defects with the deepest/longest ld.

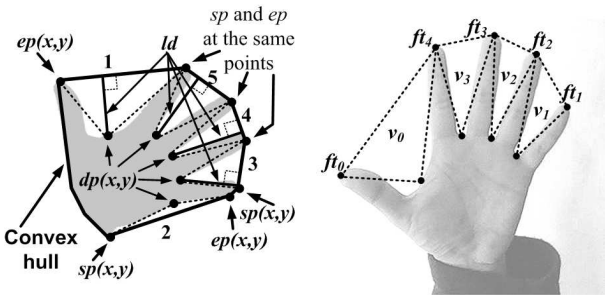

(a) (b)

Figure 3: (a) Convex hull and convexity defects of a hand; and (b) labelling fingertips and finger valleys.

4.2. Thumb Localisation and Left/Right Hand Identification

In [17], the labelling of fingertips starts with the localisation of the thumb, where the thumb tip is the fingertip that is always the farthest away from the average position of all fingertips. Once the thumb has been found, the rest of the fingertips are indexed according to their distance from the thumb tip. Our approach is slightly different to [17] by utilising the convexity defects to first locate the thumb valley and followed by the thumb tip. The subsequent process of labelling the remaining finger valleys and fingertips is presented in Section 4.3.

Assuming the hand is in outstretched position and is parallel to the image plane, the valley point $dp(x, y)$ of v_0, i.e., $v_0(dp(x, y))$, is determined by calculating the maximum accumulated distance ad between each valley point with the other three valley points, i.e.,

$$\underset{v_c}{\operatorname{argmax}}\, ad(v_c) = \sum_{i=1}^{m=3} ||v_c(dp(x, y)) - v_i(dp(x, y))|| \tag{9}$$

where $v_c(dp(x, y))$ is the current valley point being analysed, $v_i(dp(x, y))$ is the ith valley point and m is the number of valley points.

Once $v_0(dp(x, y))$ is found, the process then determines if the object is of left or right hand. The distance d_{sp} from depth point $v_0(dp(x, y))$ to start point $v_0(sp(x, y))$, and the distance d_{ep} from depth point $v_0(dp(x, y))$ to end point $v_0(ep(x, y))$ are calculated. Left hand is identified if $d_{ep} < d_{sp}$, otherwise it is a right hand. The thumb tip $ft_0(x, y)$ is assigned the end point $ep(x, y)$ or the start point $sp(x, y)$ depending on whether it is right hand or left hand, respectively.

4.3. Labelling Finger Valleys and Fingertips

Assuming v_0 is found at index k in $\bar{V}$, the remaining valleys v_i in V where $i = \{1, 2, 3\}$ are labelled using

$$v_i = \bar{v}_{((k+i) \mod 4)}. \tag{10}$$

The fingertips $FT = \{ft_i(x, y),\ i = 0, ..., 4\}$ as shown in Fig. 3(b) are labelled as follows. For left hand, the fingertips are labelled using:

- $ft_0(x, y) = v_0(ep(x, y))$
- $ft_1(x, y) = v_1(sp(x, y))$
- $ft_2(x, y) = midpoint(v_1(ep(x, y)),\ v_2(sp(x, y)))$
- $ft_3(x, y) = midpoint(v_2(ep(x, y)),\ v_3(sp(x, y)))$
- $ft_4(x, y) = midpoint(v_3(ep(x, y)),\ v_0(sp(x, y)))$.

For right hand, the fingertips are labelled using:

- $ft_0(x, y) = v_0(sp(x, y))$
- $ft_1(x, y) = v_1(ep(x, y))$
- $ft_2(x, y) = midpoint(v_2(ep(x, y)),\ v_1(sp(x, y)))$
- $ft_3(x, y) = midpoint(v_4(ep(x, y)),\ v_2(sp(x, y)))$
- $ft_4(x, y) = midpoint(v_0(ep(x, y)),\ v_3(sp(x, y)))$.

During tracking, a new fingertip measurement must be within a certain radius threshold φ (determined experimentally to be 20 pixels for image size 320x240, as larger threshold value will represent a distance too large for a finger to move to) from the previous measurement, otherwise it is considered missing and the corresponding valley structure v_i will use the previously measured $v_{i_{prev}}$. For tracking, all non-missing fingertips from FT are assigned to $FTM = \{ftM_i(x, y),\ i = 0, ..., 4\}$ indicating the measured locations of fingertips. For missing fingertips, the measurement process is presented in Section 4.6. Table 1 shows the fingertips that use their previously measured point when any or both valley depth points are missing during the current measurement.

Table 1: Measuring fingertips with missing valley depth point(s).

Valley depth point(s) missing	**Use previously measured point for**
v_0	ft_0
v_1	ft_1
v_1 and v_2	ft_2
v_2 and v_3	ft_3
v_3 and v_0	ft_4

4.4. Determining Finger Pivots

We adapt the method in [27] to determine finger pivots $PV = \{pv_i(x, y),\ i = 0, ..., 4\}$. A simpler representation is used for the pivots locations, where all finger pivots coincide with the pivot lines as shown in Fig. 4(a), whereas in [27], three finger pivots $pv_0(x, y)$, $pv_2(x, y)$ and $pv_3(x, y)$ do not. Fig. 4(a) also shows that only two middle points can be recovered, namely middle ($mid_{23}(x, y)$) and ring ($mid_{12}(x, y)$), i.e.,

- $mid_{12}(x, y) = midpoint(v_1(dp(x, y)),\ v_2(dp(x, y)))$,
- $mid_{23}(x, y) = midpoint(v_2(dp(x, y)),\ v_3(dp(x, y)))$.

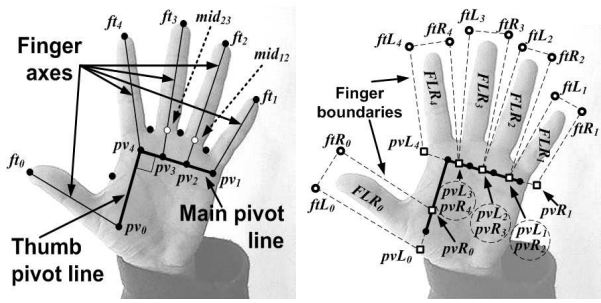

(a) (b)

Figure 4: (a) Locations of finger pivots; (b) Finger likelihood region (FLR) enclosed by finger boundaries defined by the left and right points of a fingertip and a finger valley.

The feature points, i.e., middle point between two depth point valleys, fingertips, and known pivot points, are used to estimate the pivots of all fingers. Unless otherwise specified, the pivot points are given by

$$q^* = (a - b) \times l + a, \tag{11}$$

where a and b are feature points, and the distance between two feature points $(a - b)$ is scaled by a ratio l. By considering the geometry of hand features, the different values of l are set based on the percentage difference from a to b. The process is applied to both x and y elements of each point. Pivot points $pv_1(x, y)$, $pv_2(x, y)$, $pv_3(x, y)$ and $pv_4(x, y)$ are calculated by making the following substitutions in (11):

- $q^* = pv_2,\ a = mid_{12},\ b = ft_2,\ l = 0.2$,
- $q^* = pv_3,\ a = mid_{23},\ b = ft_3,\ l = 0.2$,
- $q^* = pv_1,\ a = pv_2,\ b = pv_3,\ l = 1.2$,
- $q^* = pv_4,\ a = pv_3,\ b = pv_2,\ l = 1.2$.

$pv_1(x, y)$, $pv_2(x, y)$, $pv_3(x, y)$ and $pv_4(x, y)$ are connected to form the main pivot line (see Fig. 4(a)).

To find $pv_0(x, y)$, a temporary location is calculated similarly using (11), where $q^* = temp$, $a = pv_4$, $b = pv_3$, $l = 2.8$. This is followed by a rotation of 90° perpendicular to the main pivot line, i.e.,

$$\begin{bmatrix} pv_0(x) \\ pv_0(y) \\ 1 \end{bmatrix} = \begin{bmatrix} R_3 \end{bmatrix} \begin{bmatrix} temp(x) \\ temp(y) \\ 1 \end{bmatrix} \tag{12}$$

where

$$R_3 = \begin{bmatrix} \cos\beta & -\sin\beta & pv_4(x)(1-\cos\beta) + pv_4(y)\sin\beta \\ \sin\beta & \cos\beta & pv_4(y)(1-\cos\beta) - pv_4(x)\sin\beta \\ 0 & 0 & 1 \end{bmatrix}, \tag{13}$$

$\beta = -\frac{\pi}{2}$ for left hand and $\beta = \frac{\pi}{2}$ for right hand. pv_0 and pv_4 are connected to form the thumb pivot line (see Fig. 4(a)). When all PV and FT are extracted, all finger axes $FA = \{fa_i(x, y),\ i = 0, ..., 4\}$ are formed by connecting every fingertip ft_i with its corresponding finger pivot pv_i, denoted by fa_i.

4.5. Finger Likelihood Region

Each finger likelihood region (FLR) (see Fig. 4(b)) is used to determine whether a contour point $cp_i(x, y)$ on hand contour Q_{hand} is within a specific FLR. FLR is determined by partitioning each finger using the positions of fingertips and finger pivots. Every pivot point has its corresponding left and right points respectively denoted by $pvL_i(x, y)$ and $pvR_i(x, y)$, where $i = 0, ..., 4$ correspond to the numbering of finger pivots. $pvR_1(x, y)$, $pvL_4(x, y)$ and $pvL_0(x, y)$ are calculated by making the following substitutions in (11):

- $q^* = pvR_1$, $a = pv_1$, $b = pv_2$, $l = 0.6$,
- $q^* = pvL_4$, $a = pv_4$, $b = pv_3$, $l = 0.6$,
- $q^* = pvL_0$, $a = pv_0$, $b = pv_4$, $l = 0.4$.

For $pvR_0(x, y)$, (11) is slightly modified to $q^* = (a - b) \times l + b$, where $q^* = pvR_0$, $a = pv_4$, $b = pv_0$, $l = 0.4$. $pvL_1(x, y)$, $pvL_2(x, y)$ and $pvL_3(x, y)$ are the midpoints between two adjacent finger pivots, i.e.,

$$pvL_1 = (pv_1 + pv_2)/2, \quad pvL_2 = (pv_2 + pv_3)/2, pvL_3 = (pv_3 + pv_4)/2. \tag{14}$$

Since finger pivots $pv_1(x, y)$, $pv_2(x, y)$, $pv_3(x, y)$ and $pv_4(x, y)$ are close to each other and the palm is assumed to be a rigid object, some of $pvL_i(x, y)$ share the same point with its adjacent $pvR_{i+1}(x, y)$, i.e., $pvR_2 = pvL_1$, $pvR_3 = pvL_2$ and $pvR_4 = pvL_3$. Similar to finger pivots, every fingertip has its own left and right points denoted respectively by $ftL_i(x, y)$ and $ftR_i(x, y)$, where $i = 0, ..., 4$ correspond to the numbering of fingertips. Denote a new temporary fingertip as $ftTemp_i(x, y)$ as the location for every fingertip. $ftTemp_i(x, y)$ is located 13% (based on every finger axis length) away from its corresponding fingertip location along the finger axis, i.e.,

$$ftTemp_i = (ft_i - pv_i) \times 0.13 + ft_i. \tag{15}$$

The 13% extension is to create sufficient search space for contour points along fingertips so that the boundaries at the fingertips do not lie exactly on top of every fingertip. The line connecting $ft_i(x, y)$ and $ftTemp_i(x, y)$ is extended 120% more to create a new line connecting $ftTemp_i(x, y)$ and $temp_i(x, y)$, i.e.,

$$temp_i = (ftTemp_i - ft_i) \times 1.2 + ftTemp_i. \tag{16}$$

$temp_i(x, y)$ is rotated 90° to the left to obtain $ftL_i(x, y)$ and to the right to obtain $ftR_i(x, y)$, i.e.,

$$\begin{bmatrix} ftL_i(x) \\ ftL_i(y) \\ 1 \end{bmatrix} = \begin{bmatrix} R_3 \end{bmatrix} \begin{bmatrix} temp_i(x) \\ temp_i(y) \\ 1 \end{bmatrix} \tag{17}$$

$$\begin{bmatrix} ftR_i(x) \\ ftR_i(y) \\ 1 \end{bmatrix} = \begin{bmatrix} R_3 \end{bmatrix} \begin{bmatrix} temp_i(x) \\ temp_i(y) \\ 1 \end{bmatrix}, \tag{18}$$

where $\beta = -\frac{\pi}{2}$, and $i = 0, ..., 4$. Fig. 4(b) shows the FLR for each finger. We define the FLR as $FLR_i = \{pvL_i(x, y),\ pvR_i(x, y),\ ftL_i(x, y),\ ftR_i(x, y)\}$, comprising four points that define the boundaries, where $i = 0, ..., 4$ corresponds to the finger number.

A separate image I_{FLR} is created with the same size as the input image frame I_{bp}. I_{FLR} is used as a lookup table to determine every cp_i should they fall into any FLR_i. I_{FLR} array is first set to zero. Once an FLR_i is determined, every pixel in I_{FLR} which corresponds to a pixel enclosed by FLR_i is set to i. This results in every finger region having pixel value that corresponds to the finger number.

4.6. Fingertip Measurement during Finger Bending

Precise fingertip measurement during finger bending is not practical for a real-time application and using only skin colour segmentation will fail to track the edge of a fingertip while it is bending. We thus propose Algorithm 4 as an approximate solution to fingertip measurement during finger bending.

In Algorithm 4, all contour points cp_m of hand contour Q_{hand} are evaluated, and in each iteration, every two consecutive contour points $cp_{cur}(x, y)$ and $cp_{next}(x, y)$ are extracted. Pixel value at $cp_{next}(x, y)$ in I_{FLR} is stored in val_1. For every fingertip in FT, if val_1 contains a value i (indicating that $cp_{next}(x, y)$ is within FLR_i), and if ft_i uses its previous values, then the line ln_{cur} connecting $cp_{cur}(x, y)$ and $cp_{next}(x, y)$ is evaluated to determine if it intersects with the corresponding finger axis fa_i. The pixel locations in I_{FLR} that correspond to the pixel locations along line ln_{cur} are first set to a value k. Define the following determinants:

$$A = \begin{vmatrix} a & b \\ c & d \end{vmatrix}, \quad B = \begin{vmatrix} e & f \\ g & h \end{vmatrix}, \quad C = \begin{vmatrix} a & 1 \\ c & 1 \end{vmatrix}, \tag{19}$$

Algorithm 4 Finding fingertips during bending.

```
for each cp_m(x, y) in Q_hand, m = 1, ..., N do
    cp_cur(x, y) = cp_m(x, y)
    cp_next(x, y) = cp_{m+1}(x, y)
    ln_cur =from cp_cur(x, y) to cp_next(x, y)
    val_1 =get pixel value from I_FLR at point cp_next(x, y)
    for each ft_i(x, y) in FT, i = 0, ..., 4 do
        if val_1 = i AND ft_i(x, y) uses previous value then
            set I_FLR to k for all pixels along ln_cur
            ip(x, y) = intersection point of ln_cur and fa_i axis
            if ip(x, y) within I_FLR frame then
                val_2 =get pixel value from I_FLR at point ip(x, y)
                if val_2 = k then
                    ftM_i(x, y) = ip(x, y)
                end if
            end if
        end if
    end for
end for
```

$$D = \begin{vmatrix} b & 1 \\ d & 1 \end{vmatrix}, \quad E = \begin{vmatrix} e & 1 \\ g & 1 \end{vmatrix}, \quad F = \begin{vmatrix} f & 1 \\ h & 1 \end{vmatrix}, \tag{20}$$

where $cp_{cur}(x, y) = (a, b)$, $cp_{next}(x, y) = (c, d)$, $ft_i(x, y) = (e, f)$ and $pv_i(x, y) = (g, h)$. The intersection point $ip(x, y)$ between the line ln_{cur} and finger axis fa_i is

$$ip(x) = \frac{\begin{vmatrix} A & C \\ B & E \end{vmatrix}}{\begin{vmatrix} C & D \\ E & F \end{vmatrix}}, \quad ip(y) = \frac{\begin{vmatrix} A & D \\ B & F \end{vmatrix}}{\begin{vmatrix} C & D \\ E & F \end{vmatrix}} \tag{21}$$

The resulting $ip(x, y)$ is for the infinitely long lines, i.e., an intersection point can occur beyond the two line segments. To determine whether $ip(x, y)$ lies on both line segments, a pixel value in I_{FLR} corresponding to the position $ip(x, y)$ is extracted and stored temporarily in val_2. If val_2 is the same as k then $ip(x, y)$ is said to lie on both line segments ln_{cur} and fa_i. The measured fingertip is stored as $ftM_i(x, y)$. Fig. 5 illustrates a hand contour with the index finger while bending. Note that $v_3(dp(x, y))$ is missing and only

$v_0(dp(x,y))$, $v_1(dp(x,y))$ and $v_2(dp(x,y))$ are measured.

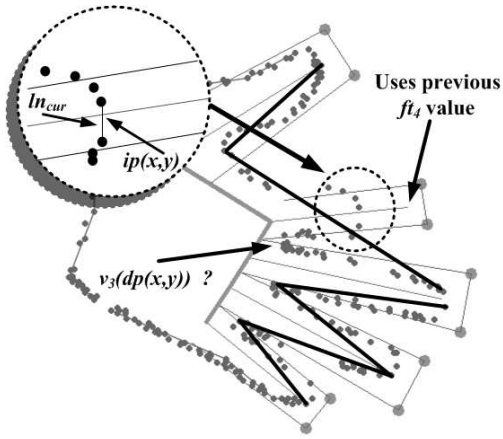

Figure 5: A hand contour showing the index finger while bending. Fingertip ft_4 uses the previously measured value. The top left circle shows an enlarged version of the edge of the bending finger. ln_{cur} is the line connecting two consecutive contour points, and $ip(x,y)$ is the intersection point between ln_{cur} and the finger axis.

5. Hand Tracking Framework

GOPF is applied after the features extraction process to maintain the stability of the tracking of fingertips, especially during noisy measurements or occlusion. A validation gate mechanism is used in Algorithm 5 as a means to detect outliers in the measurement of ft_i such as missing or misplaced features during measurements. Validation gate radius $vgate_i$ (initially set to 20 pixels for image size 320x240) for fingertip i is introduced to check if the distance between newly measured ft_{i_t} and the previously measured $ft_{i_{t-1}}$ is less than $vgate_i$. If ft_{i_t} is accepted, $vgate_i$ is reduced as well as ensure that the reduction does not fall below the validation gate threshold τ_{vgate} (normally set to 20 pixels). On the other hand, if the distance is greater than $vgate_i$, the validation gate $vgate_i$ is increased. The increment of $vgate_i$ is checked to ensure that it is no larger than 4 times the validation gate threshold τ_{vgate}. At this point, the newly measured ft_i is invalidated and considered to be an outlier since it is too far from the previous measurement. Therefore, ft_i has to use the current state estimation $\hat{s}_t$. When this occurs, the fingertip i is in occlusion or currently experiencing noisy measurement. The increase in the size of $vgate_i$ will be used in the next measurement in new frame in order to enlarge the search space.

After ft_i is updated in Algorithm 5, and if fingertip i is in occlusion, ft_i is again iteratively checked against the extracted contour to search for the closest contour peak to ft_i that is within τ_{vgate} radius. If a peak is found, ft_i is updated to that peak.

Algorithm 5 Outliers detection with validation gate.

```
for each ft_i, i = 0, ..., 4 do
    if distance(ft_{i_t}, ft_{i_{t-1}}) < vgate_i then
        vgate_i = vgate_i − (τ_vgate/2)
        if vgate_i < τ_vgate then
            vgate_i = τ_vgate
        end if
    else
        vgate_i = vgate_i + (τ_vgate/2)
        if vgate_i > (τ_vgate × 4) then
            vgate_i = τ_vgate × 4
            ft_i = ŝ_t
        end if
    end if
end for
```

6. Experimental Results

A synthetic experiment is used to compare the performance of GOPF with PF [7]. A simulation of a nonlinear movement is used to compare GOPF with variants of PF. The robustness of the proposed hand tracking algorithm is validated using real hand video sequences, where comparison is also carried out with state-of-the-art CAMSGPF. Occlusion handling performance is also performed on both synthetic and real video sequences. All experiments are performed on Intel Core 2 Duo 2 GHz processor with 4GB RAM. OpenCV 2.1 is used as the programming environment.

6.1. Synthetic Experiment

A simple mouse tracker program is developed for which PF [7] and GOPF are applied to track the mouse movement as shown in Fig. 6. This experiment is performed in order to find the best parameter settings for GOPF to achieve robust performance. Fig. 7 shows the performance of PF and GOPF with different threshold τ values. It shows that GOPF outperforms PF for all values of τ, and $\tau = 0.2$ gives its best performance where the average error decreases as the number of particles increases. As the number of particles increases, $\tau < 0.2$ results in degraded performance because more particles are replicated using Algorithm 1 instead of Algorithm 2. For $\tau > 0.2$, the opposite happens. Larger τ values tend to give better results, but most replicated particles would be too concentrated at the true posterior, which results in low samples diversity. Thus, $\tau = 0.2$ is used for GOPF for the remaining experiments in this paper.

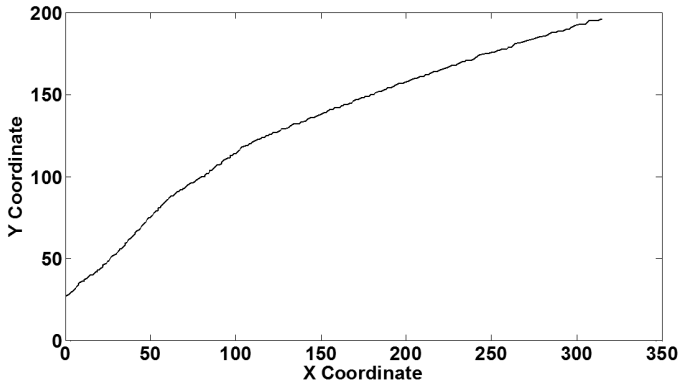

Figure 6: Mouse movement used in a synthetic experiment.

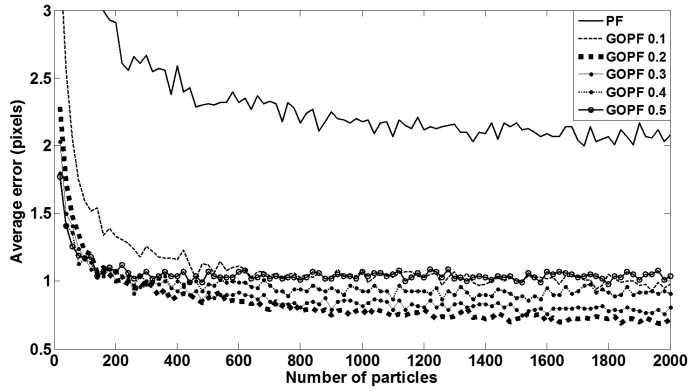

Figure 7: Performance of PF and GOPF in tracking mouse movement.

We simulate a random mouse movement (comprising 3,717 frames) where the mouse moves from different directions and going through a virtual square-shaped occlusion located at the centre of the screen as shown in Fig. 8. There are no measurements whenever the mouse enters the virtual occlusion. We compare PF using 100 particles against GOPF using 20 particles and threshold $\tau = 0.2$ on occlusions handling. The high peaks of the results in Fig. 9 indicates that the mouse is entering the virtual occlusion, and that GOPF outperforms PF during occlusion. The average error in the first 200 frames just before the first occlusion is 3.62 for PF and 3.03 for GOPF. Even without the occlusion, GOPF with 20 particles still performs better than PF with 100 particles. Fig. 10 shows the tracking estimation results of PF and GOPF between frames 200 and 300 which corresponds to the first peak in Fig. 9. Immediately after entering the occlusion boundary, PF tends to get stuck at the last known measurement and slowly drifts downwards but still within the vicinity of the last known measurement as shown in Fig. 10. GOPF however produces more reasonable tracking prediction using the last known mouse movement drift. It tends to follow the actual mouse movement even though there are no measurements during occlusion.

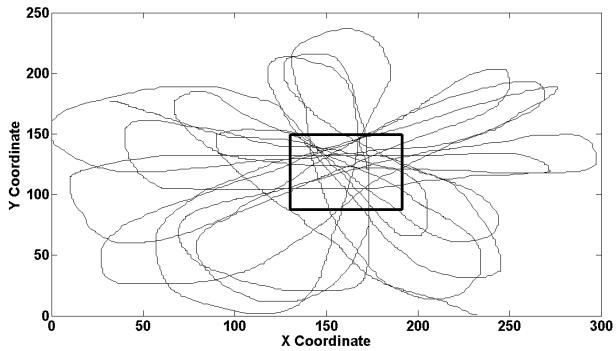

Figure 8: Random mouse movement passing through a virtual square-shaped occlusion.

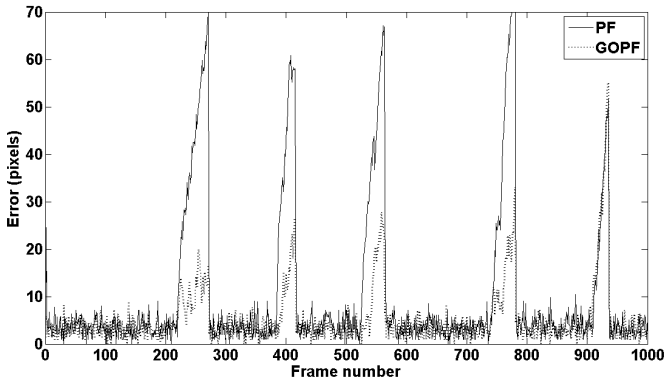

Figure 9: Tracking errors of PF and GOPF during occlusion.

6.2. Simulation

We compare the performance of GOPF with several variants of particle filters namely extended Kalman filter (EKF) [28], sampling importance resampling PF (SIRPF) [29], auxiliary PF (APF) [30], and regularised PF (RPF) [31] using the nonlinear movement of an object whose position is represented by [32]

$$x_t = \frac{x_{t-1}}{2} + \frac{25x_{t-1}}{1 + x_{t-1}^2} + 8\cos(1.2(t-1)) + w_t, \tag{22}$$

and

$$y_t = \frac{x_t^2}{20} + j_t, \tag{23}$$

where w_t and j_t are zero mean Gaussian random variables with variances 10 and 1, respectively, representing a severely nonlinear model. The works in [33, 29, 34, 21] use this movement to evaluate the performance of various particle filter algorithms. Root Mean Squared Error (RMSE) is used as a quantitative measure of performance. All variants including GOPF use 100 particles. The results in Table 2 are obtained by averaging the RMSE errors over 100 runs for each variant. We also added 5%, 10%, 15% and 20% zero mean Gaussian noise levels to the original data to evaluate the performance of the various methods in the

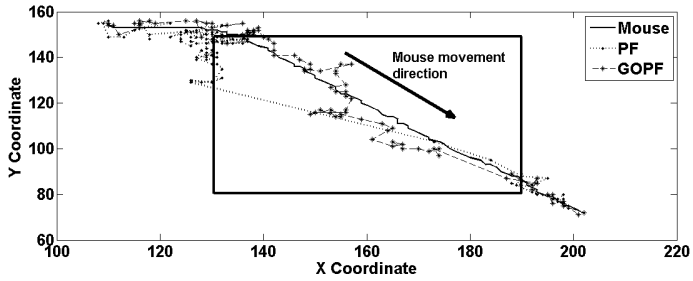

Figure 10: Tracking estimation of PF and GOPF between frames 200 and 300 of the random mouse movement.

presence of different noise levels. Although the performance of GOPF degrades with increasing noise level, Table 2 shows that GOPF consistently and significantly outperforms all other algorithms at all noise levels. Consistent with the results demonstrated in [21], APF always shows slightly better performance compared to SIRPF and RPF, whereas SIRPF and RPF always show comparable performance.

Table 2: RMSE performance of variants of particle filter with different noise levels.

Algorithm	**0%**	**5%**	**10%**	**15%**	**20%**
EKF	23.88	30.48	46.48	53.15	62.91
SIRPF	5.58	6.23	7.84	8.59	9.74
APF	5.19	6.04	7.16	7.96	9.05
RPF	5.24	6.37	7.89	8.51	9.69
GOPF	4.49	5.24	6.41	7.19	8.42

6.3. Qualitative Analysis

A real video sequence is used to evaluate the proposed hand tracking framework. The sequence comprises 416 frames of 320x240 colour images running at 30 fps of a hand with the palm parallel to the camera image plane, and captured using Logitech Quickcam 3000. In this sequence, each finger is bending one at a time starting with the thumb, followed by index, middle, ring and pinky. The first frame shows the hand with all fingers in stretched position. A small region of skin colour is manually sampled in the first frame to be used for skin colour segmentation in the subsequent frames. In the first frame, all finger valleys and fingertips are identified and labelled using the methods in Section 4.1 to Section 4.5. GOPF using 20 particles and $\tau = 0.2$ is then applied to track every fingertip in the subsequent frames where it is observed that the tracking operates at the video rate of 30 fps. Fig. 11 shows some qualitative comparisons of hand tracking using PF [7] and GOPF. Note that the measurement noise causes the measured fingertips to not lie exactly at the actual positions. The result using GOPF optimises the tracking towards the true posterior with an equivalent performance of PF using 1000 particles.

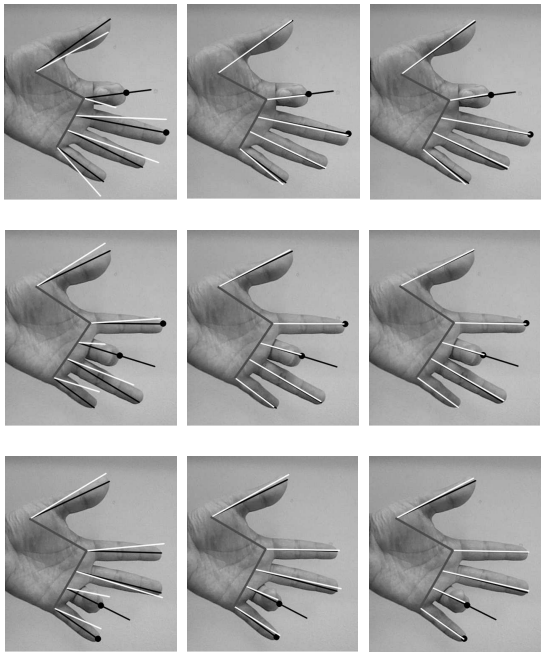

Figure 11: First, second and third row are results from frame 129, 221, and 295, respectively. Left column shows example of hand tracking using PF with 10 particles, middle column are the corresponding results using GOPF with 20 particles, and right column shows the corresponding results using PF with 1000 particles. White lines denote the predicted positions and black lines denote the measured positions. Black circles denote the fingers entering the missing mode and the fingertips are measured using Algorithm 4.

GOPF is also applied to a sequence in [35]. This sequence comprises 600 frames of 228x284 colour images of hand bending one finger at a time starting from thumb, followed by index, middle, ring and pinky. Our hand tracking framework is able to track the whole sequence reliably. Fig. 12(a) shows the sequence at frame 326 where the middle finger is bending with all other fingers successfully tracked. Pinky and ring fingers appear closer towards each other, merging them to a single contour as shown in Fig. 12(b). However, the tracking framework is still able to track the two fingers separately.

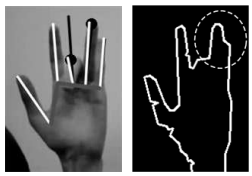

(a) (b)

Figure 12: (a) Frame 326 of the sequence in [35]. (b) The corresponding hand contour for frame 326. The white dashed circle shows merged contour for pinky and ring fingers.

6.4. Hand Tracking: PF vs. GOPF

To validate the performance of GOPF quantitatively, the same sequence as in Fig. 11 is used to compare its tracking results against the ground truth. Since it is difficult to obtain ground truth data for real hand video sequence, a common approach [16][35] to a quantitative evaluation of hand tracking is to use a manually annotated ground truth. Every fingertip is manually annotated and stored in $FTGT = \{ftGT_i(x, y),\ i = 0, ..., 4\}$. Fig. 13 shows the average error of tracking the five fingers, defined as

$$\text{average error} = \sum_{i=0}^{4} \frac{|ftM_i - ftGT_i|}{5}. \tag{24}$$

where ftM_i are the positions of fingertips determined by PF [7] or GOPF. Clearly, GOPF with fewer than 50 particles far outperforms PF with more than 1000 particles. According to [20, 16], and as shown by our experiment, increasing the number of particles does not improve the accuracy significantly.

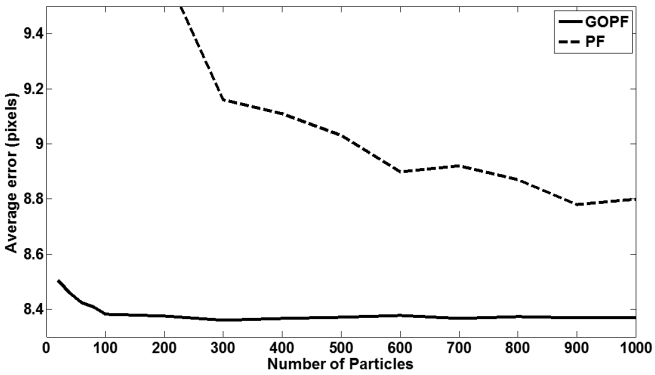

Figure 13: Performance of PF and GOPF in hand tracking.

6.5. GOPF vs. PF and CAMSGPF

GOPF is further compared with PF [7] and CAMSGPF [11]. Using the state vector of every propagated particles as the measurement vector, CAMSGPF works by re-applying or re-measuring the current image using the simplified CamShift, moving every particle close to the true local mode. GOPF attracts nearby propagated particles towards the true local mode using gravitational concept without involving any re-measurement. As reported in [11], CAMSGPF using only 10 particles shows comparable performance with PF using 100 particles. We applied CAMSGPF using 10 particles to track a moving hand in a real video sequence comprising 80 frames as shown in Fig. 14. The hand is moving from the right to the left of the frame.

The result in Fig. 15 shows the comparable performance of CAMSGPF using 10 particles and PF using 100 particles. It is clear that PF using only 10 particles performs worst. Some significant spikes can be seen in the results of CAMSGPF at frames 2 to 4 and at frames 44 to 58, whereas PF using 100 particles shows

Figure 14: A frame in the video sequence of a hand moving from right to left.

considerable stability. The same pattern can be seen in the tracking result on the hockey sequence in [11], where CAMSGPF shows some fluctuations at frames 400 to 450 of the sequence. This shows some slightly poor performance of CAMSGPF using 10 particles than with PF using 100 particles in term of stability. Fig. 15 shows GOPF with 10 particles is more stable compared to PF using 100 particles. The average errors in tracking are 5.2 for CAMSGPF using 10 particles, 13.6 for PF using 10 particles, 4.2 for PF using 100 particles, and 4.1 using GOPF. The poor performance in the average error of CAMSGPF is partly due to its optimisation process that might converge into false local mode.

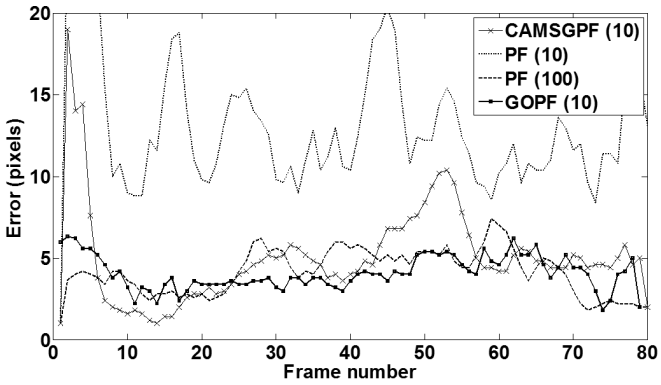

Figure 15: Performance of GOPF vs. CAMSGPF and PF in tracking video sequence in Fig. 14.

6.6. Hand tracking under different hand movements

The performance of the hand tracking framework in tracking a long video sequence comprising 924 frames of different hand movements is also evaluated. The sequence starts with the hand moving closer and slowly moving farther away from the camera, and then back to its original position. This type of movement has the effect of scaling the object larger or smaller. The hand then moves up and down which shows the object translation from one position to another. All these movements maintain the palm to be parallel to the camera. The movements right after this point do not maintain the palm parallel to the camera. The wrist is bent forward and backward, moving the fingertips closer and farther away from the camera, respectively. The movement is stopped when the wrist has turned roughly 45° during forward or backward movement. The whole hand is than twisted forward and backward moving the thumb closer and farther away

from the camera, respectively. Again, the movement is limited to twisting the hand at roughly 45° during forward or backward movement. Fig. 16 shows the framework is able to track all movements successfully and reliably, where the predicted positions of fingers (denoted by white lines) coincide with the measured positions (denoted by black lines).

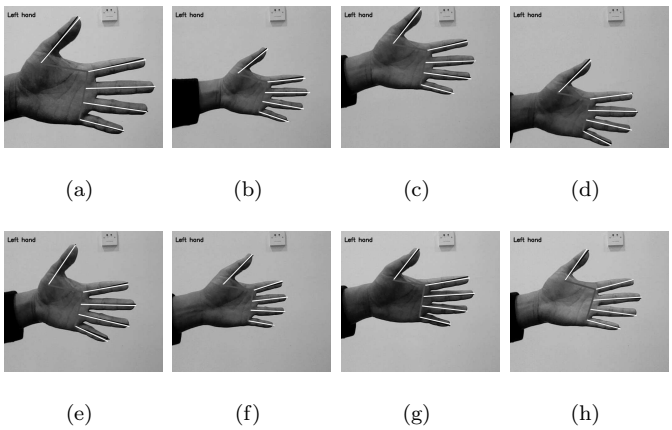

Figure 16: Performance of GOPF in tracking different type of hand movements in a single video sequence: (a) moving closer and (b) moving farther from camera; (c) moving up and (d) down; (e) bend hand forward; (f) bend hand backward; (g) twist hand with thumb forward; and (h) twist hand with thumb backward. White lines denote the predicted positions and black lines denote the measured positions.

6.7. Hand tracking in challenging environment

The performance of GOPF with 20 particles to track hand movement in cluttered background is evaluated. The video sequence used in this experiment comprises 710 frames of size 320x240, where a hand enters the scene performing various movements that involve scaling, rotation and translation. The result in Fig. 17 shows successful tracking of the hand throughout the video sequence.

GOPF is also evaluated with a more challenging environment in a video sequence containing 585 frames of size 320x240, where the background as well as the foreground contain skin coloured objects. The foreground contains left and right hands where each hand moves closer towards the camera interchangeably. In this sequence, GOPF is used to track the left hand. Fig. 18 shows the results of the hand tracking. Initially, only the left hand is present and is tracked as shown in frame 24. In frame 158, the right hand enters the scene and as the right hand moves closer towards the camera, its contour becomes the largest skin coloured blob to be detected. However, the hand tracking framework is able to maintain lock on the left hand. In frames 162 and 432, the left hand contour are distorted by a skin coloured background. However, the hand tracking framework successfully maintains correct tracking of the hand in these frames. The results on this sequence demonstrate the ability of GOPF to successfully track the hand under significant illumination changes especially when the hand moves closer or away from the camera, i.e., even though deformed hand

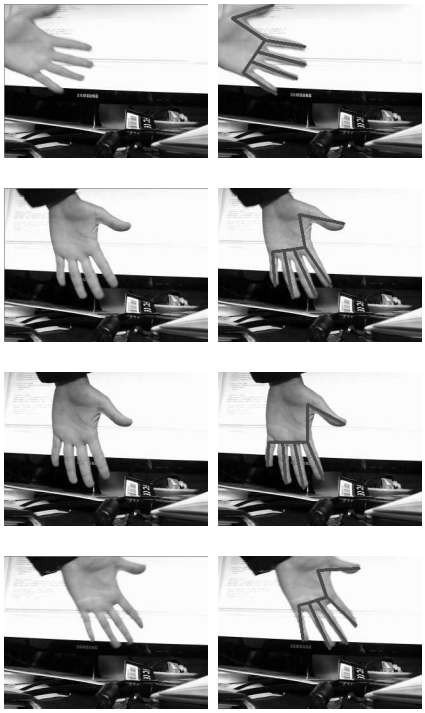

Figure 17: Hand tracking in cluttered environment. First to fourth rows are results from frame 48, 484, 496 and 598, respectively. Left column shows the frames and right column shows the frames with the results (i.e., black lines superimposed onto the frames) of the hand tracking using GOPF with 20 particles.

contours are extracted.

6.8. Occlusion handling

To evaluate the performance of GOPF with 20 particles for occlusion handling in real image video, a sequence comprising 319 frames of left hand moving randomly and being occluded twice by an object is used. Fig. 19 shows the results where frame 101 shows the tracking before the occlusion. The circle on each fingertips shows the validation gate. At frame 101, the validation gates are at their minimum radius of 20 pixels. As the occlusion occurs in frame 107, all fingers cannot be measured and the validation gates for all fingertips increase. As the occlusion disapears in frame 119, fingertips pinky, ring, and middle have fully recaptured new measurements and their validation gates return to minimum radius. Index fingertip is still minimizing the validation gate, while thumb fingertip has just recovered new measurement. When the occlusion completely dissapears at frame 121, almost all fingertips' validation gates have returned to minimum radius.

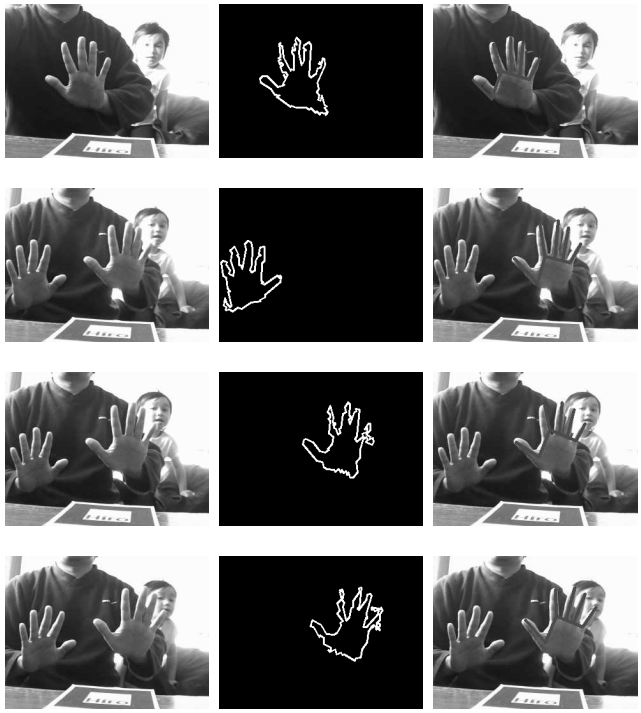

Figure 18: Hand tracking in the presence of other skin-colour objects. First row to fourth row are results from frame 24, 158, 162 and 432, respectively. The left column shows the actual frame, the middle column shows the detected contour of the hand, and the right column shows the results (i.e., black lines superimposed onto the frames) of the hand tracking using GOPF with 20 particles.

7. Conclusions

In this paper, we propose a novel tracking algorithm GOPF by incorporating PF and the replication of new particles based on gravitational attraction which improves the sampling efficiency as well as significantly reducing the required number of particles compared to PF. The hand features extraction algorithm which utilises the convex hull and the convexity defects of the hand shape robustly detects and labels each finger, as well as identifying if they are of the left or right hand. In terms of accuracy, the GOPF based tracking outperforms the PF based tracking including various well known variants of PF such as EKF, SIRPF, APF and RPF. GOPF also outperforms the state-of-the-art CAMSGPF algorithm in terms of stability. Integration and animation with an OpenGL hand model is the focus of future work where the use of stereo imaging technique will be incorporated to increase the accuracy of 3D pose estimation. The proposed GOPF based hand tracking framework has several limitations, and are subject to improvement in future works. The hand features extraction method may fail in the event the palm twists more than 45°. Complete occlusion for a longer period of time might cause the tracker to fail. Fewer parameters usage is preferable in hand features extraction to avoid missing many parts of the parameters during extraction. Lastly, threshold parameters

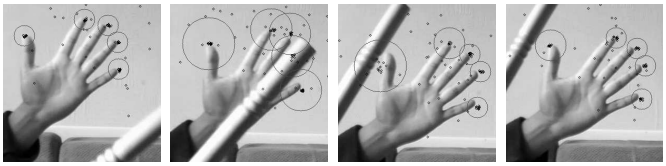

(a) (b) (c) (d)

Figure 19: Performance of GOPF in occlusion handling. The results from left to right are from frames 101, 107, 119, and 121 of the sequence. The circle on each fingertip shows the validation gate. The validation gate increases when occlusion occurs, and decreases when new measurement is found.

are set in pixels unit and mostly work for image size of 320x240. Although threshold parameters can be adjusted for different image sizes, it is not intended to be used for this framework as it may degrade the speed (when using large image size) or the accuracy (when using small image size) of the tracking framework.

Acknowledgments

The authors would like to thank the Ministry of Higher Education Malaysia and International Islamic University Malaysia for providing the funds for this research.

References

[1] H. Francke, J. Ruiz-del Solar, R. Verschae, Real-time hand gesture detection and recognition using boosted classifiers and active learning, in: D. Mery, L. Rueda (Eds.), Advances in Image and Video Technology, Vol. 4872 of Lecture Notes in Computer Science, Springer Berlin / Heidelberg, 2007, pp. 533–547.

[2] X. Chai, Y. Fang, K. Wang, Robust hand gesture analysis and application in gallery browsing, in: Proceedins of IEEE International Conference on Multimedia and Expo, Vol. 1 - 3, 2009, pp. 938 –941.

[3] R. Y. Wang, J. Popović, Real-time hand-tracking with a color glove, ACM Transactions on Graphics 28 (2009) 63:1–63:8.

[4] D. Lee, Y. J. Lee, Framework for vision-based sensory games using motion estimation and collision responses, IEEE Transactions on Consumer Electronics 56 (3) (2010) 1356 –1363.

[5] A. Chan, H. V. Leong, S. H. Kong, Real-time tracking of hand gestures for interactive game design, in: Proceedings of IEEE International Symposium on Industrial Electronics, 2009, pp. 98 –103.

[6] A. Erol, G. Bebis, M. Nicolescu, R. D. Boyle, X. Twombly, Vision-based hand pose estimation: A review, Journal on Computer Vision and Image Understanding 108 (1-2) (2007) 52 – 73.

[7] M. Isard, A. Blake, Condensation - conditional density propagation for visual tracking, Internationa Journal on Computer Vision 29 (1998) 5–28.

[8] M. Isard, A. Blake, Icondensation: Unifying low-level and high-level tracking in a stochastic framework, in: Proceedings of the 5th European Conference on Computer Vision, Vol. I, 1998, pp. 893–908.

[9] M. Bray, E. Koller-Meier, L. Van Gool, Smart particle filtering for high-dimensional tracking, Journal on Computer Vision and Image Understanding 106 (2007) 116–129.

[10] C. Shan, T. Tan, Y. Wei, Real-time hand tracking using a mean shift embedded particle filter, Pattern Recognition 40 (2007) 1958–1970.

[11] Z. Wang, X. Yang, Y. Xu, S. Yu, Camshift guided particle filter for visual tracking, Pattern Recognition Letters 30 (2009) 407–413.

[12] I. Oikonomidis, N. Kyriazis, A. Argyros, Efficient model-based 3d tracking of hand articulations using kinect, in: Proceedings of the 22nd British Machine Vision Conference, BMVA, University of Dundee, UK, Aug. 29-Sep. 1, 2011, pp. 101.1–101.11.

[13] W.-Y. Chang, C.-S. Chen, Y.-D. Jian, Visual tracking in high-dimensional state space by appearance-guided particle filtering, IEEE Transactions on Image Processing 17 (7) (2008) 1154 –1167.

[14] J. Romero, H. Kjellstrom, D. Kragic, Monocular real-time 3d articulated hand pose estimation, in: Proceedings of the 9th IEEE-RAS International Conference on Humanoid Robots, 2009, pp. 87 –92.

[15] Y. Wu, J. Lin, T. Huang, Analyzing and capturing articulated hand motion in image sequences, IEEE Transactions on Pattern Analysis and Machine Intelligence 27 (12) (2005) 1910 –1922.

[16] N. Stefanov, A. Galata, R. Hubbold, A real-time hand tracker using variable-length markov models of behaviour, Computer Vision Image Understing 108 (2007) 98–115.

[17] Y. Shen, S. K. Ong, A. Y. C. Nee, Vision-based hand interaction in augmented reality environment, International Journal on Human-Computer Interaction.

[18] T. E. Homma K, An image processing method for feature extraction of space-occupying lesions, Journal of Nuclear Medicine 26 (1985) 1472–1477.

[19] J. Deutscher, I. Reid, Articulated body motion capture by stochastic search, International Journal on Computer Vision 61 (2005) 185–205.

[20] M.-F. Ho, C.-Y. Tseng, C.-C. Lien, C.-L. Huang, A multi-view vision-based hand motion capturing system, Pattern Recognition 44 (2011) 443–453.

[21] M. Arulampalam, S. Maskell, N. Gordon, T. Clapp, A tutorial on particle filters for online nonlinear non-gaussian bayesian tracking, IEEE Transactions on Signal Processing 50 (2) (2002) 174 –188. doi:10.1109/78.978374.

[22] K. A. R. L. Pearson, The Problem of the Random Walk, Nature 72 (1867) (1905) 342.

[23] I. Cohen, A. Whitman, I. Newton, The Principia Mathematical Principles of Natural Philosophy, University of California Press, 1999.

[24] G. Bradski, A. Kaehler, Learning OpenCV: Computer Vision with the OpenCV Library, O'Reilly, Cambridge, MA, 2008.

[25] D. H. Douglas, T. K. Peucker, Algorithms for the reduction of the number of points required to represent a digitized line or its caricature, Cartographica: The International Journal for Geographic Information and Geovisualisation 10 (2) (1973) 112–122.

[26] J. Sklansky, Finding the convex hull of a simple polygon, Pattern Recognition Letters 1 (2) (1982) 79 – 83.

[27] E. Yoruk, E. Konukoglu, B. Sankur, J. Darbon, Shape-based hand recognition, IEEE Transactions on Image Processing 15 (7) (2006) 1803 –1815. doi:10.1109/TIP.2006.873439.

[28] H. W. Sorenson, Kalman filtering: theory and application., IEEE, 1985.

[29] N. Gordon, D. Salmond, A. Smith, Novel approach to nonlinear/non-gaussian bayesian state estimation, IEEE Proceedings F, Radar and Signal Processing 140 (2) (1993) 107–113.

[30] M. K. Pitt, N. Shephard, Filtering via Simulation: Auxiliary Particle Filters, Journal of the American Statistical Association 94 (446) (1999) 590–599.

[31] C. Musso, N. Oudjane, F. Legland, Improving regularized particle filters, in: A. Doucet, N. de Freitas, N. Gordon (Eds.), Sequential Monte Carlo Methods in Practice. New York, springer-verlag Edition, Statistics for Engineering and Information Science, 2001, pp. 247–271.

[32] G. Kitagawa, Non-gaussian state-space modelling of non-stationary time series (with discussion), Journal of the American Statistical Association 82 (1987) 1032–1063.

[33] N. G. P. Bradley P. Carlin, D. S. Stoffer, A Monte Carlo Approach to Nonnormal and Nonlinear State-Space Modeling, Journal of the American Statistical Association 87 (418) (1992) 493–500.

[34] G. Kitagawa, Monte carlo filter and smoother for non-gaussian non-linear state space models, Journal of Computer Graphics and Statistics 5 (1) (1996) 1–25.

[35] M. de La Gorce, D. Fleet, N. Paragios, Model-based 3d hand pose estimation from monocular video, IEEE Transactions Pattern Analysis and Machine Intelligence (2011) to be published.